Sensors & Actuators: B. Chemical 419 (2024) 136409

Contents lists available at ScienceDirect

Sensors and Actuators: B. Chemical

journal homepage: www.elsevier.com/locate/snb

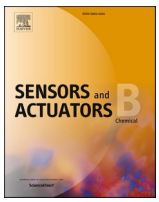

Facile E-nose based on single antenna and graphene oxide for sensing volatile organic compound gases with ultrahigh selectivity and accuracy

Yu Dang [a,*], Yenugu Veera Manohara Reddy [b], Michael Cheffena [a]

[a] Faculty of Engineering, Norwegian University of Science and Technology, Gjøvik 2815, Norway
[b] Department of Chemistry, Sri Venkateswara College (University of Delhi), New Delhi 110021, India

ARTICLE INFO

Keywords:
Electronic-nose
Graphene oxide
Isomeric volatile organic compound
Machine learning
Communication capacity

ABSTRACT

Volatile organic compounds (VOCs) gases exist as important indicators in various processes such as human breath, food spoilage, plant disease, and industrial production, which makes VOC sensing a promising nondestructive detection method. Nanomaterial enabled electronic noses (e-noses) are gaining increasing attention for their exceptional ability to distinguish between multiple VOCs. To achieve this, multiple sensors with distinct nanomaterials are crucial for providing enough diversity for successful discrimination. Apparently if e-nose can be implemented solely on single sensor with single common nanomaterial operating at room temperature, the complexity and power consumption can be greatly decreased. In this study, a significant milestone is achieved as, for the first time, a single antenna sensor coated with commercial graphene oxide, demonstrates comparable performance to array-based e-noses, and even outperforms them in terms of the ultimate ambition of selectivity—isomeric VOC classification. An impressive classification accuracy of 96.7 % is attained for multiple VOC gases, including isomers. Additionally, the concentration of each component in VOC isomer mixtures is accurately determined. Unlike conventional antenna sensors, the sensor maintains stable communication during sensing operations. Finally, the practical feasibility of the antenna e-nose (Ant-nose) is successfully demonstrated with a series of food quality assessments.

1. Introduction

VOC gas sensing, as a promising nondestructive detection technology finds diverse applications in agriculture [1], environmental protection [2], fruit freshness [3], meat spoilage [4], disease diagnosis [5], and public safety [6]. In practical applications, diverse VOCs may share similar characteristics but have distinct levels of toxicity or impact on humans and the environment [7], necessitating discrimination between multiple VOC analytes. Additionally, it is common for multiple VOCs to coexist as indicators, evident in scenarios such as postharvest fruit damage [8], fruit ripening [3,9], and plant disease diagnosis [10]. Furthermore, the real-life detection process can be complicated by potential interference from irrelevant VOCs. Faced with these challenges, depending on sensors that detect only a specific VOC is impractical. Reliable and robust detection is achieved only through the collective analysis of a panel of VOCs, creating distinct 'fingerprints' of the sample under test.

To meet practical requirements, the nanomaterials-enabled electronic nose (e-nose), inspired by mammalian olfaction [11], stands out as a promising biomimetic device [12–14]. Comprising an array of sensors, each coated with a distinct nanomaterial, the e-noses demonstrate affinity to a range of VOCs, yielding diverse response levels. These responses are collectively processed using a pattern recognition algorithm, resembling the human brain [4]. Attributed to the variety of the sensors in e-nose, profiling the distinct pattern and classification of analytes under test can be achieved. Various transducers and sensitive materials have been extensively explored and applied for e-nose. Taking some state-of-art works as example, Capman et al. introduced a graphene e-nose with 432 sensors, functionalized with 36 distinct receptors, achieving an 89 % discrimination accuracy among 6 different VOCs at 4 concentrations each [15]. Similarly, Kybert et al. introduced a graphene e-nose with 56 sensors functionalized by 4 DNA oligomers, visually separating 8 chemical vapors [16]. Weerakkody et al. presented a five-element biohybrid e-nose effectively discriminating 4 VOCs [11]. Wang et al. introduced a semiconductor metal oxide (SMO) e-nose with 5 sensors made up of 5 types of zinc oxide, achieving 99 % classification accuracy among 6 VOCs [17].

However, use of multiple transducers and sensitive nanomaterials in

* Corresponding author.
E-mail address: yu.dang@ntnu.no (Y. Dang).

https://doi.org/10.1016/j.snb.2024.136409
Received 10 January 2024; Received in revised form 17 May 2024; Accepted 1 August 2024
Available online 2 August 2024

e-nose significantly increases complexity, power consumption, and overall size. To ensure sufficient diversity for profiling the fingerprint pattern of analytes, many sensors coated with either distinct nanomaterials [18] or the same base nanomaterial functionalized differently [15,16,19], are required thus necessitate complex and time-consuming preparation. Multiple sensors also necessitate additional supporting circuitry and infrastructure for powering and multichannel data acquisition [13]. For some SMO and micro-LED based e-noses, extra thermal activation or photoactivation also adds up to the power consumption [18,19]. The breakdown or malfunction of a single element in the system can lead to the failure of the entire system. In practical applications, such as wireless sensor networks (WSNs) requiring large-scale sensor deployment, the application of e-noses is hindered by cost and complexity. Moreover, the feasibility of the above-mentioned e-noses in real-life scenarios remains unverified, with isomer detection achieved by only one graphene e-nose [15]. Differentiating between VOC isomers, as the ultimate goal for e-nose selectivity, remains a challenging task due to the exceptionally high molecular similarities.

Hence if we can achieve e-nose functionality with single sensor and a common nanomaterial, the system can be significantly simplified, leading to a drastic reduction in complexity, power consumption, and overall size. To this aim, the cross-sensitivity of nanomaterial towards multiple VOCs is necessary. Graphene oxide (GO), as a crucial member of two-dimensional (2D) materials, meets the criteria of cross-sensitivity, room temperature operation, and commercial availability, making it popular for VOC sensing [20–23]. Apart from nanomaterial, transducer is another important composition of e-nose. The antenna sensor, a key member of microwave sensors, offers the potential for a single-sensor-based e-nose due to its inherent multiple resonances. These resonances, separated by several gigahertz (GHz) within the microwave band, can enable the profiling of distinct fingerprints for different analytes. Moreover, the IoT's rapid growth requires sensor nodes with both sensing and communication functions [24,25]. An antenna sensor simplifies design by eliminating the need for an extra antenna [26]. However, existing antenna sensors have limitations, such as communication performance always get affected during sensing, necessitating additional compensation circuitry, as proposed by our group [27,28]. It's essential to note that no research on an antenna-based e-nose has been conducted thus far.

In this work, we introduce the Ant-nose for the first time—a single antenna-based e-nose. Deposited with commercial graphene oxides without functionalization as a cross-selective receptor as illustrated in Fig. 1, the Ant-nose can be prepared through a facile procedure. It achieves VOC discrimination and concentration regression, even in the presence of isomers and isomer blends at the ppm level. By leveraging the reflection coefficient at various resonances across an ultra-wide microwave frequency spectrum, the Ant-nose generates effective multidimensional 'fingerprints' for VOC discrimination. In our measurements, it accurately differentiates six VOC types, including 2 pairs of isomers, with a remarkable 96.7 % classification accuracy. Additionally, the Ant-nose determines concentrations in binary VOC isomer mixtures with an R-squared value exceeding 0.98. Its stable communication capability during VOC detection further highlights its effectiveness. Finally, the Ant-nose demonstrates its feasibility in real-life scenarios, including measurements of fruit and meat freshness, and apple mechanical damage detection. Some other potential applications are also illustrated in Fig. 1. This Ant-nose showcases the possibility of achieving multi-sensor based e-nose functionality using a single sensor and simple procedures, promising potential for next-gen e-nose development.

2. Experimental section

2.1. Fabrication and measurement of antenna

The proposed novel Ant-nose is designed with Ansys® high-frequency structure simulator (HFSS). Fig. 1 shows the geometric

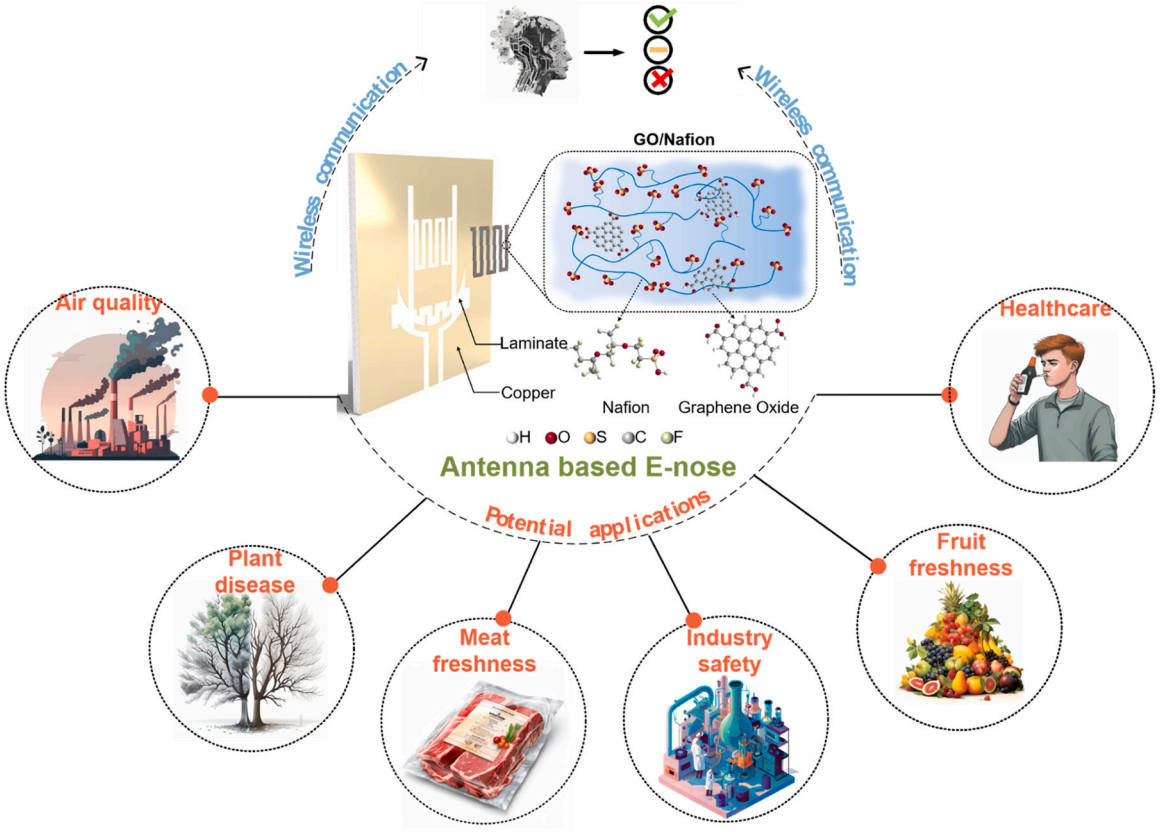

Fig. 1. Architecture, composition, and potential applications of the proposed Ant-nose.

topology of the Ant-nose. The integration of sensing and communication functions is achieved on a coplanar waveguide (CPW) fed PCB board with an overall size of 33×33 mm. Design principle is detailed in Section 3.4. Detailed dimensional information is given in Fig. S1 and Table S1. All dimensional parameters are kept to one decimal place for ease of mechanical processing. Then the antenna was etched on a Roger® RO4003C copper clad laminate with a dielectric constant of 3.38 and thickness of 1.524 mm. The etching process, carried out with the LPKF® ProtoMat S64 (Fig. S2), used a cost-effective milling method to produce precise structures as small as 100 μm. Then the fabricated antenna was polished with sandpaper to remove potential surface oxidation layer, and a SMA connector was soldered at the CPW port. Measurement of reflection coefficient was done with a Rohde & Schwarz® Vector Network Analyzer ZVA67. As shown in Fig. S3, ultra-wide microwave band from 1 to 8 GHz was swept. The radiation measurements were conducted using a near-field multi-probe system, specifically our MVG® StarLab (Fig. S4).

2.2. Sensitive nanomaterial coating

The sensitive layer was made of graphene oxide/Nafion composite as illustrated in Fig. 1. Nafion serves as both a backbone for supporting and binding GO together, as well as reducing charge transfer resistance to facilitate VOC molecule detection [29,30]. Other advantages of GO and Nafion are detailed in Note S1. 4 mL GO dispersion in water with a concentration of 4 mg mL^{-1} was mixed with 1 mL anhydrous ethanol and 2 mL Nafion® perfluorinated resin solution (5 wt%), followed by 30 minutes ultrasonication. Subsequently, a tailored mask was affixed to the Ant-nose. Then 0.2 mL above mentioned dispersion was spray-coated onto Ant-nose under 0.2 MPa pressure and 10 cm distance. The Ant-nose was subsequently left in ambient condition for 40 minutes to evaporate solvent, resulting in the formation of a thin sensing membrane. To assess the sensing performance using an alternative sensitive material, 16 mg graphite was mixed with 5 mL anhydrous ethanol and 2 mL Nafion® perfluorinated resin solution (5 wt%). This mixture underwent a 72 hour magnetic stirring process followed by 2 hours of ultrasonication. Then the drop coating was performed with 0.1 mL graphite-Nafion solution, followed by 30 minutes evaporation in ambient condition. Fig. S5 shows the photographs of Ant-nose after coating. All above-mentioned chemicals and solvents are purchased from Sigma–Aldrich® and used without further purification.

2.3. VOC sensing with ant-nose

The complete experimental setup is shown in Fig. 2A. A gas tight container (EM-Tec Save-Storr, from Micro-to-Nano®) with available volume of 10 L was used as our home-made gas chamber, similar like setups used in other researches [31–33]. To establish a connection between the VNA and Ant-nose, a coaxial cable was secured through a hole in the chamber's side wall. A 5200 rpm fan is placed inside chamber to stir and homogenize VOC gas distribution. The Ant-nose in chamber is connected to a vector network analyzer (VNA) via the coaxial cable. To stabilize conditions inside the chamber, the fan is switched on and the lid and valve of the chamber are closed 10 minutes before each measurement. During measurement anhydrous VOC liquid including methanol (MeOH), 1-proponal (PrOH), 2-proponal (IPA), 2-butanol (2BuOH), 1butanol (BuOH), and ethanol (EtOH) (>99.5 %, from Sigma-Aldrich®) with specific volume are injected with precise gas tight sampling syringe (10–100 μL, from Hamilton® and SGE®) through the ball valve of gas chamber. Note that the inside diameter of the valve is almost the same as outside diameter of the syringe so that leakage during injection is minimized. With known gas chamber volume, the relationship between the VOC concentration and the volume of the VOC liquid can be found using specific equation [31–34]. Detailed volume-concentration calculations are given in Note S2 and Table S2. The VNA, controlled by MATLAB code running on a laptop, measures and stores reflection coefficient (S11) of the Ant-nose every second. Within 1–8 GHz microwave frequency band, totally 1333 frequency points are used. To extract features from measurement with higher dimensionality, we use both real and imaginary parts of S11, as depicted in Fig. S3. Every time after the injection of VOC liquid the valve is closed immediately, then after 10 mins measurement the lid of chamber is opened to refresh the chamber with a fume hood. All experiments were conducted under ambient conditions at about 20°C and 40 % humidity, similar conditions to our group's previous work [35,36]. For each concentration, the response is calculated by averaging five repeated measurements.

3. Results and discussion

3.1. Discrimination of individual VOCs including isomers

For individual VOC tests, concentrations ranging from 200 ppm to 1000 ppm (with 200 ppm interval) were measured for each of the six different VOCs. After measurements, we select five peaks/valleys in real part (Re2–2.77 GHz, Re5–4.67 GHz, Re6–4.93 GHz, Re9–6.69 GHz, Re10–6.83 GHz) and six peaks/valleys in imaginary part (Im2–2.61 GHz, Im3–2.87 GHz, Im5–4.45 GHz, Im6–4.81 GHz, Im7–5.08 GHz, Im10–6.78 GHz) that exhibit the highest variation as shown in Fig. S3. This totally yields 11 features collected at distinct frequencies. The average response of the last 10 seconds of measurement at each frequency point was used as a feature. Fig. S6 showcases the response curves at 11 selected frequencies for 6 VOCs. Notably, some curves show an increase with concentration, while others exhibit a decrease. To visualize the unique response fingerprint for the 6 VOCs, response curves are plotted in polar coordinates in Fig. 2B, with 11 features represented by angles and different concentrations distinguished by colors. These fingerprints intuitively discriminate between different VOC types. In summary, the study involved measuring six distinct VOCs, with five different concentrations tested for each VOC, resulting in 30 observations. Each observation was characterized by 11 features. To address potential limitations due to limited data, augmentation techniques, specifically the Synthetic Minority Over-sampling Technique (SMOTE), were employed (detailed in Note S3). Through SMOTE, the total number of observations was increased to 120. To identify different VOC types quantitatively, the eXtreme Gradient Boosting (XGBoost) machine learning algorithm was applied (depicted as Fig. 2C, detailed in Note S3).

To reduce less informative features, we performed principal component analysis (PCA) before applying XGBoost. Subsequently, the first five principal components (PCs), explaining 99.9 % of the variance, were used as input for XGBoost (see Note S3). In the analysis of four VOC types (MeOH, PrOH, BuOH, EtOH) without isomers, the 3D PCA plot (Fig. 2D) exhibits clear separability, with data points of the same VOC type aligning along a straight line, demonstrating the Ant-nose's discriminative capability. Leveraging the XGBoost model with 75 % of the data as training data and reserving 25 % as test data, we attained a 100 % classification accuracy and a 97.5 % cross-validation accuracy for the four VOCs without isomers (first two panels of Fig. 2E). Leave-one-out cross-validation (LOOCV) was employed due to limited sample quantity [37](detailed in Note S3). In addition to classification, we conducted multivariate linear regression of PC1-PC4 against the concentration of each VOC gas to predict concentrations (see Note S4). LOOCV was used to validate the regression performance. The final panel of Fig. 2E demonstrates that predicted concentrations in cross-validation closely align with true concentrations. Calculated R-squared and adjusted R-squared values surpass 0.99 for all VOCs, indicating strong linearity between the Ant-nose's response and concentrations in a multidimensional space.

The inclusion of isomers complicates distinguishing between multiple VOCs. The six VOCs in our study are MeOH, PrOH, BuOH, 2-BuOH, IPA, and EtOH, wherein PrOH and IPA are isomers, as are BuOH and 2-BuOH. In Fig. S7, the 3D PCA plot for all six VOC types reveals slight

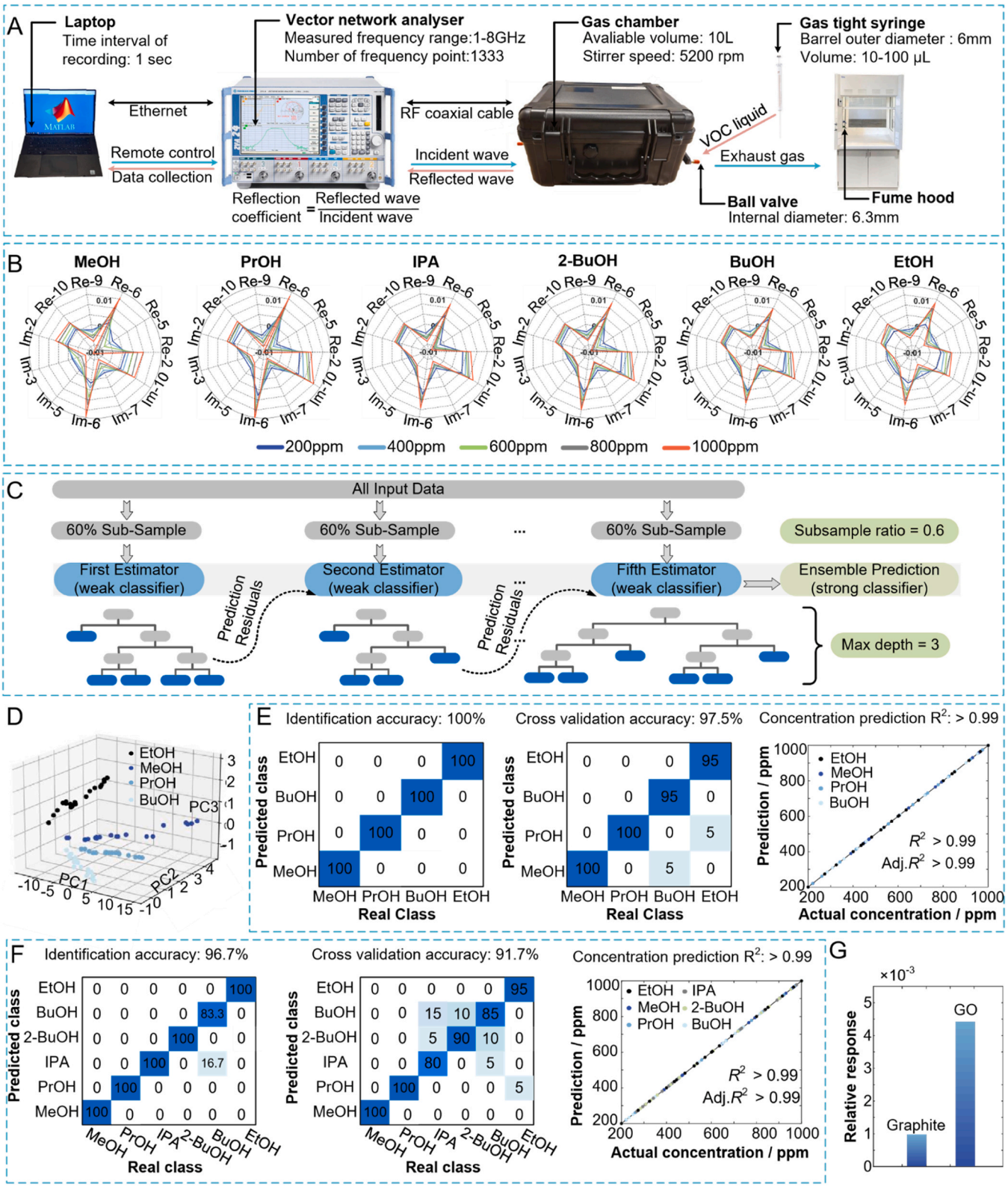

Fig. 2. A) Experimental setup and specifications for VOC vapor sensing. B) Fingerprint of six VOC gases, featuring 11 real and imaginary S11 features at various frequencies. C) Schematic diagram of the eXtreme Gradient Boosting (XGBoost) algorithm. D) 3D plot of the first 3 principal components from PCA results for four VOCs without isomers. E) Classification and concentration prediction results for four VOCs without isomers, including identification, cross-validation, and linear regression. F) Results for six VOCs with isomers, including identification, cross-validation, and linear regression. G) Sensor response to 500 ppm EtOH exposure with the Ant-nose coated with different sensitive materials.

overlap among scatter points corresponding to IPA, BuOH, and 2-BuOH. Hence, relying solely on PCA results is insufficient for discriminating effectively, prompting us to use the first 5 PCs for the XGBoost classification model. As depicted in the first two panels of Fig. 2F, considering all six VOC types, we achieve a satisfactory classification accuracy of 96.7 % and a cross-validation accuracy of 91.7 %. Notably, the second panel of Fig. 2F reveals a slight cross-sensitivity of our sensor towards IPA, BuOH, and 2-BuOH, consistent with observations in the 3D PCA plot (Fig. S7), where these VOCs exhibit overlapping tendencies. In the third panel of Fig. 2F, cross-validation results for concentration prediction show R-squared and adjusted R squared values exceeding 0.99 for all six VOCs. These results emphasize the sensor's exceptional capability to accurately differentiate between various VOCs, even in the presence of isomers. Our proposed Ant-nose leverages the intrinsic cross-sensitivity of the nanomaterial, providing additional advantages to increase feature dimensionality. Moreover, the versatility of the Ant-nose was demonstrated by using graphite (Fig. 2G) as an alternative chemiresistive material (see Note S6).

Additionally, the influence of humidity and short-term repeatability was experimentally investigated. The response of Ant-nose (Im10) to 200 ppm and 400 ppm 2-BuOH at different humidity levels is shown in Fig. 3A. As RH increases, the error bars, representing the standard deviation of five measurements, begin to overlap between two concentrations. This indicates that higher humidity increases measurement uncertainty. Thus, at low RH (21 % - 55 %), the Ant-nose maintains a relatively stable response, but at higher RH, the uncertainty is too high to discriminate between adjacent concentrations. Besides, our sensor showed good short-term repeatability (Fig. 3B) despite slight humidity fluctuations(Fig. S8). Finally, the theoretical limit of detection (LOD) for VOCs was calculated using the formula: $LOD = 3 \times \sigma/S$ [31,38], where σ represents the standard deviation at zero concentration (1.7×10^{-4}, see Fig. 3C) and S denotes the average sensitivity from 0 to 200 ppm, approximated due to non-linear responses in Fig. S6. The LOD value of each VOC was determined by comparing and finding the lowest estimated LOV over 11 feature frequencies, as highlighted in Table 1, and the LOD of Ant-nose is comparable to conventional sensor array based e-nose systems (detailed in Note S5 and Table S5).

Table 1
Estimated LOD, all LOD value in ppm.

	MeOH	PrOH	IPA	2-BuOH	BuOH	EtOH
LOD (Re2)	67.8	30.2	34.8	46.2	47.7	126.6
LOD (Re5)	47.8	22.5	20.9	26.9	30.8	180.9
LOD (Re6)	**42.2**	17.4	19.4	24.7	27.9	**55.8**
LOD (Re9)	72.3	28.7	35.2	45.0	50.0	95.8
LOD (Re10)	77.5	41.9	42.4	48.7	64.7	146.8
LOD (Im2)	111.4	47.5	55.9	75.9	87.5	165.0
LOD (Im3)	105.7	49.3	50.2	69.5	80.5	175.2
LOD (Im5)	108.2	51.7	62.9	71.0	85.0	168.1
LOD (Im6)	54.7	**15.2**	**16.3**	**19.4**	**21.6**	63.4
LOD (Im7)	65.9	29.6	32.5	41.4	44.3	143.2
LOD (Im10)	74.4	18.8	20.4	25.4	29.2	123.5

3.2. Discrimination of VOC isomer mixture

In this section, our goal is to determine the concentration of each component in binary VOC isomer gas mixtures, specifically the 1/2-propanol and 1/2-butanol mixtures. Existing research on isomeric VOC identification with complex array-based e-noses has been limited to discriminating individually present isomers or between binary mixtures with selected ratios (e.g., 1:1 or 1:3), without providing accurate concentration information for each VOC in the binary mixture [39,40]. To address this challenge, we select a total of 12 frequencies (Re2–2.77 GHz, Re5–4.67 GHz, Re6–4.93 GHz, Re7–5.31 GHz, Re9–6.69 GHz, Re10–6.83 GHz, Im2–2.61 GHz, Im3–2.87 GHz, Im5–4.45 GHz, Im6–4.81 GHz, Im7–5.08 GHz, Im10–6.78 GHz) for regression analysis of both 1/2-propanol and 1/2-butanol mixtures, as presented in Figs. S9 and S10. Given the complexity of this task, more features are required compared to the previous section that discriminated single VOCs. For each of the 12 frequency points, we select 100 data points as features, yielding 12 vectors with 100 elements each. These elements represent sequential measurements taken over the first 300 seconds, with one point recorded every 3 seconds. The arrangement of the 100 points in each vector follows the chronological order of the testing time. Due to the limited sample quantity, we implemented SMOTE for both components in the binary mixture. Initially, the original measurements comprised 25 observations, with each component measured from 100 ppm to 500 ppm, at intervals of 100 ppm. Following SMOTE for both VOC components, the total number of observations increased to 175. Given the above sequence of vectors as input, a Transformers model-based regressor can be a suitable candidate for capturing the dependencies and patterns within and across the frequency points and the time-ordered measurements. A schematic diagram in Fig. 4A illustrates the structure of our custom Transformer regressor (detailed in Note S3).

We used mean squared error (MSE) as the evaluation metric and loss function during the model training process, as plotted in the third panel of Fig. 4B. From the training loss curve, we can conclude that our model is learning to predict as expected. The testing loss curve shows that the generalization performance also increasing during training. Furthermore, as shown in the first two panel of Fig. 4B, most points align on the diagonal, confirming accurate predictions by the trained model. The calculated R squared values are 0.982 and 0.989 for 1-Propanol and 2-Propanol in the mixture, respectively. Moreover, an additional experiment involving a binary mixture of 1-Butanol and 2-Butanol was also conducted. In third panel of Fig. 4C, the loss function stabilizes at very low values after 150 epochs for both the test and training sets in the experiment. As shown in the first two panels of Fig. 4C, the predictions closely match the actual concentrations, resulting in calculated R-squared values of 0.986 and 0.983 for 1-Butanol and 2-Butanol, respectively. These findings underscore the Ant-nose's precision in

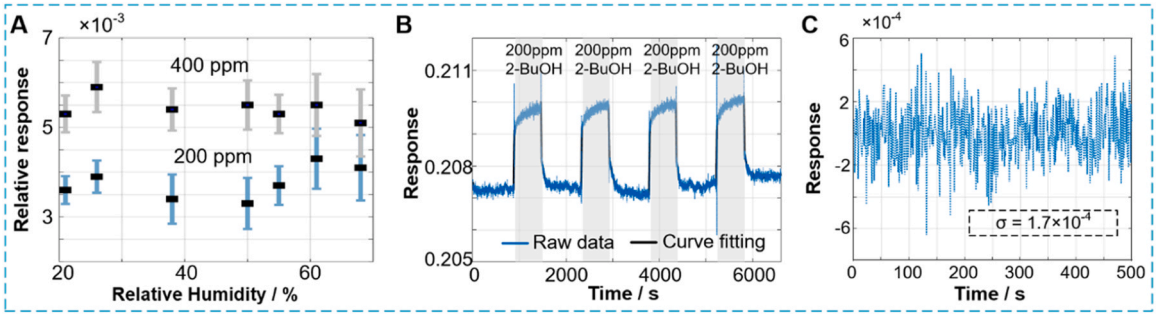

Fig. 3. A) Response to 2-BuOH (200 and 400 ppm) across humidity levels; error bars show standard deviation of five measurements. B) Short-term repeat test of the proposed Ant-nose upon exposure of 200 ppm 2-BuOH. C) Noise level at zero VOC concentration.

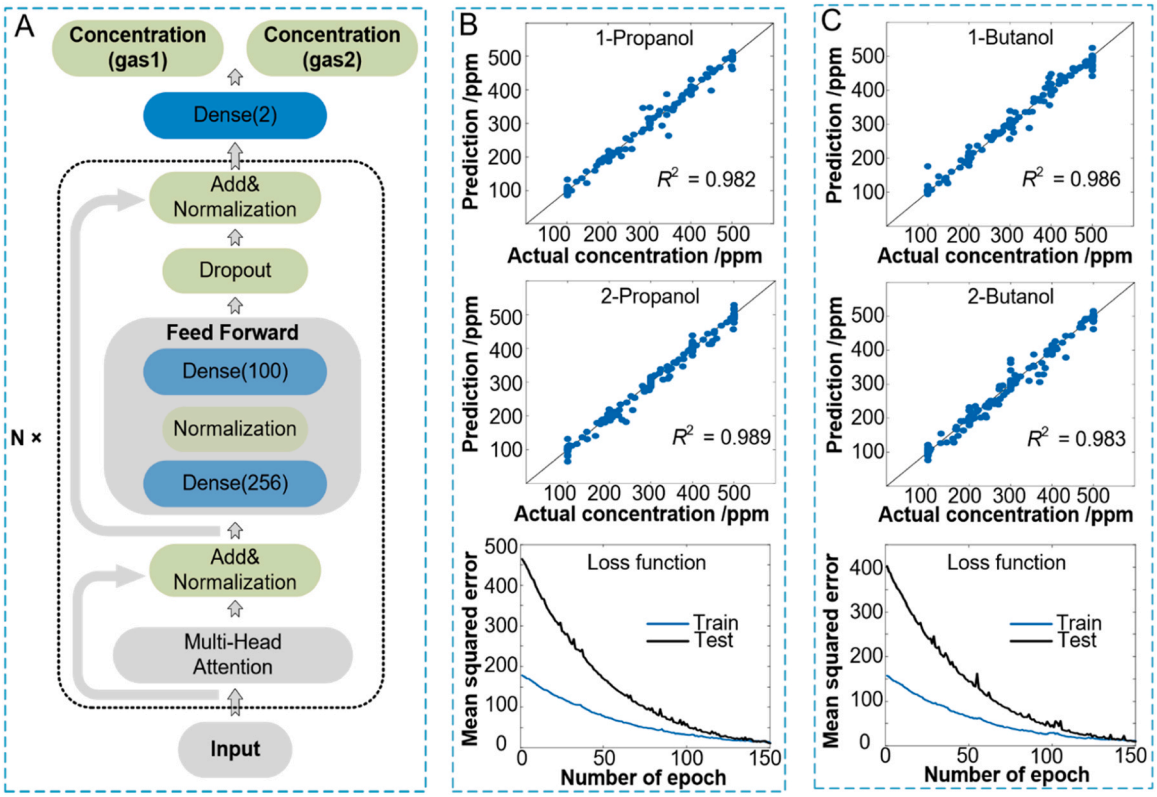

Fig. 4. A) Schematic diagram of the transformer model used in this work. B) Regression result of 1/2-Propanol mixture. Top: concentration prediction of 1-Propanol. Middle: concentration prediction of 2-Propanol. Bottom: model MSE as a function of number of epochs. C) Regression result of 1/2-Butanol mixture. Top: concentration prediction of 1-Butanol. Middle: concentration prediction of 2-Butanol. Bottom: model MSE as a function of number of epochs.

determining the concentration of each component in binary VOC isomer gas mixtures.

3.3. Food quality measurement with Ant-nose

Real-life applications pose greater complexity than laboratory settings, as multiple VOC markers can coexist and undergo simultaneous variations in a single event [3,8–10]. While sensor-array-based e-noses have demonstrated the ability to distinguish individual VOCs, their practical feasibility in real-world scenarios remains unvalidated [15,16,18]. Food quality inspection is a crucial real-life application of VOC detection due to the strong link between food quality and the composition of released aromas or flavors [41–43]. Traditional food evaluation is costly and labor-intensive, relying on manual inspection [44,45], while VOC detection offers a nondestructive, cost-effective alternative for efficient evaluation. To validate our Ant-nose in real-life scenarios, we measured food freshness (grape, strawberry, and pork) and detected mechanical damage in apples.

Firstly, damage in apples is assessed. Throughout the postharvest supply chain, factors like impact, compression, and vibration can easily result in fruit damage. Once got mechanical damage, the market value of fruits decreases not only due to oxidation browning, water losses and decline in firmness [46] but also because the fruits become more vulnerable to bacterial and fungal infections [47]. According to some research [9,48,49], noticeable changes in the concentration of multiple VOCs can be observed once fruits undergo damages. Therefore, VOC detection plays a vital role in fruit damage evaluation, contributing to optimize the fruit storage, transportation, and sales strategies. In our measurement, to simulate the compression damage incurred by static loads on apples in postharvest supply chain, artificial damage was induced using a small hammer. Four circular regions on each apple were subjected to similar pressure within the equatorial zone of the fruits as denoted by the white circles in Fig. 5A. It is important to note that this pressure did not breach the skin of the apples. Five apples were damaged and another five were left untouched to serve as the control group as shown in Fig. 5B. All apples from the same brand were bought together at the local supermarket. Subsequently, two sets of apples were placed at 10°C for a duration of 12 hours before analysis. Following this storage period, the areas of the apple that had undergone pressure exhibited a darker hue compared to the surrounding regions. Then all apple samples were individually assessed. Each apple underwent an 8-minute measurement with our Ant-nose, followed by an additional 8 minutes for gas chamber purging. The heatmaps in Figs. 5C and 5D, representing eight distinct features (re2, re5, re6, re9, im3, im5, im6, im7) with the most significant variations, effectively demonstrate the differentiation between the two groups. Moreover, the t-SNE analysis in Fig. 5E further confirms this distinction in a two-dimensional feature space, highlighting the sensor's ability to discern apples with damage based on VOC release.

Besides damage in fruit, given that each type of fruit possesses a distinctive aroma comprising hundreds of VOCs, and considering that various categories of VOCs, including alkenes, esters, aldehydes, and alcohols, are linked to fruit freshness, the assessment of VOCs has emerged as a pivotal approach for freshness inspections [3]. In our study, strawberries and grapes were used for fruit freshness evaluation. Fruits from the same brand were purchased both five days and one day prior to the measurement, stored at 10°C. After five days, four strawberries exhibited varying darkening, while the last one exhibited no noticeable change, revealing ripeness variations even within the same fruit box (Fig. 6A). Subsequently, employing the same measurement procedure as for damaged apples, we assessed ten strawberries. Figs. 6B and 6C illustrate clear differences between fresher and five-day-old strawberries. T-SNE analysis in Fig. 6E further confirmed the distinction. Similar assessments were made for two grape groups (Figs. 7A and

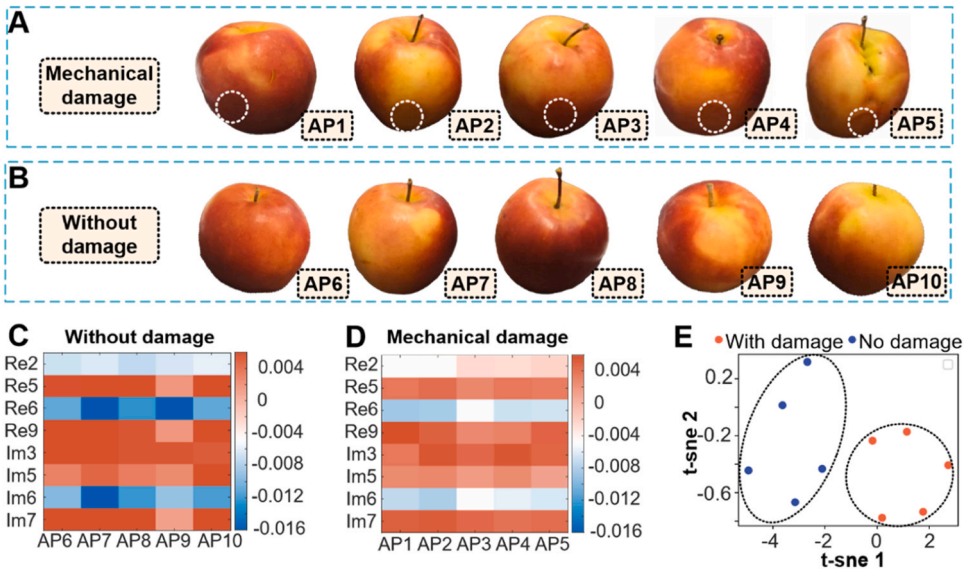

Fig. 5. A) Apples with artificial damage on surface denoted by the white circles. B) Another five healthy apples used as the control group. C) Heatmap made up of eight selected features for healthy apples. D) Heatmap for damaged apples. E) t-SNE results with clear separation between two groups of apples.

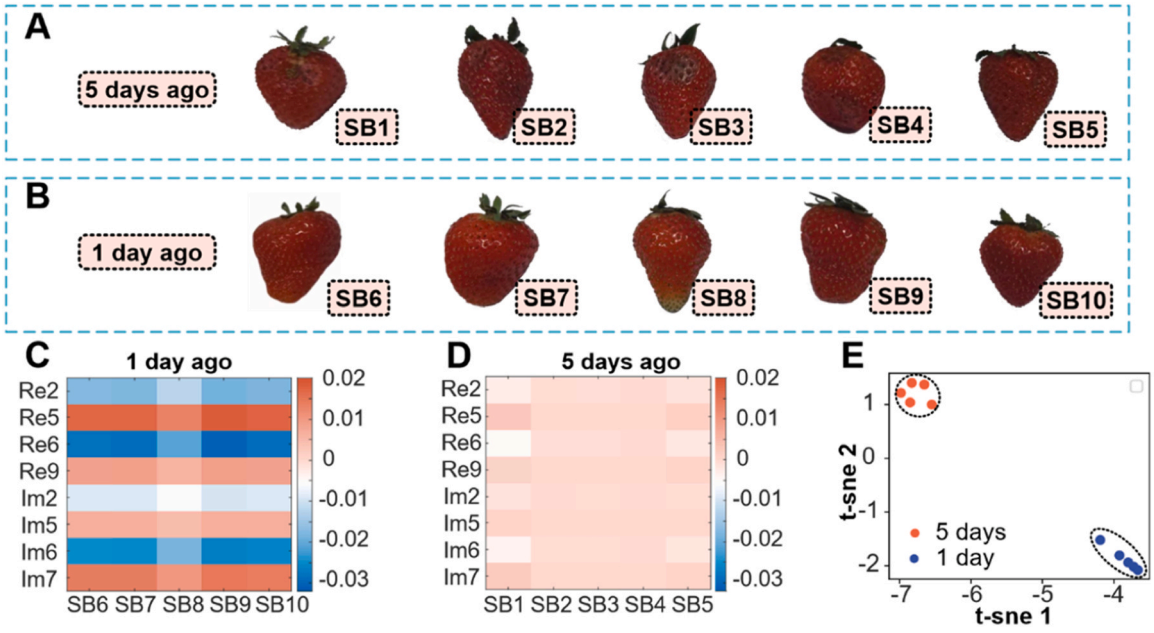

Fig. 6. A) Strawberries bought 5 days before measurement. B) Strawberries bought 1 day before measurement. C) Heatmap made up of eight selected features for one-day ago strawberries. D) Heatmap for five-days ago strawberries. E) t-SNE results with clear separation between two groups of strawberries.

7B), revealing size differences in the older grapes. Heatmaps (Figs. 7C and 7D) and t-SNE (Fig. 7E) analysis showed distinct separations.

Finally, we extended our assessment to meat freshness—another critical application of VOC detection [50]. We assessed meat freshness by cutting two groups of pork (bought 5 days ago and 1 day ago) into small pieces (Figs. 8A and 8B). The heatmap in Figs. 8C and 8D represents eight selected features, and the t-SNE result in Fig. 8E shows clear but less pronounced separation than other tests. This may be due to the nanomaterial used here being less responsive to VOCs associated with pork freshness.

3.4. Ant-nose communication stability during sensing

In Fig. 9A, the function of each component of the Ant-nose is illustrated, highlighted by different colored boxes. Detailed information about the equivalent function within each box is provided in Note S7. Fig. 9B shows the reflection coefficient of the Ant-nose during 1000 ppm EtOH detection, with different-colored curves for various operation times. Notably, the amplitudes of the 2 resonances at 2.77 GHz and 4.76 GHz increase with time as circled in the black boxes, while the amplitude of the communication resonance (5.72 GHz) remains constant. The communication resonance at 5.72 GHz exhibits a −10 dB bandwidth of 380 MHz (5.53–5.91 GHz), effectively covering the world widely used 5.8 G ISM band (5.725–5.875 GHz) [51–53]. In Fig. 9C, examining resonance amplitude stability during the detection of six VOCs at different concentrations reveals that unlike the other 2 resonances, the communication resonance remains unchanged, demonstrating the Ant-nose's fixed communication band unaffected by VOC

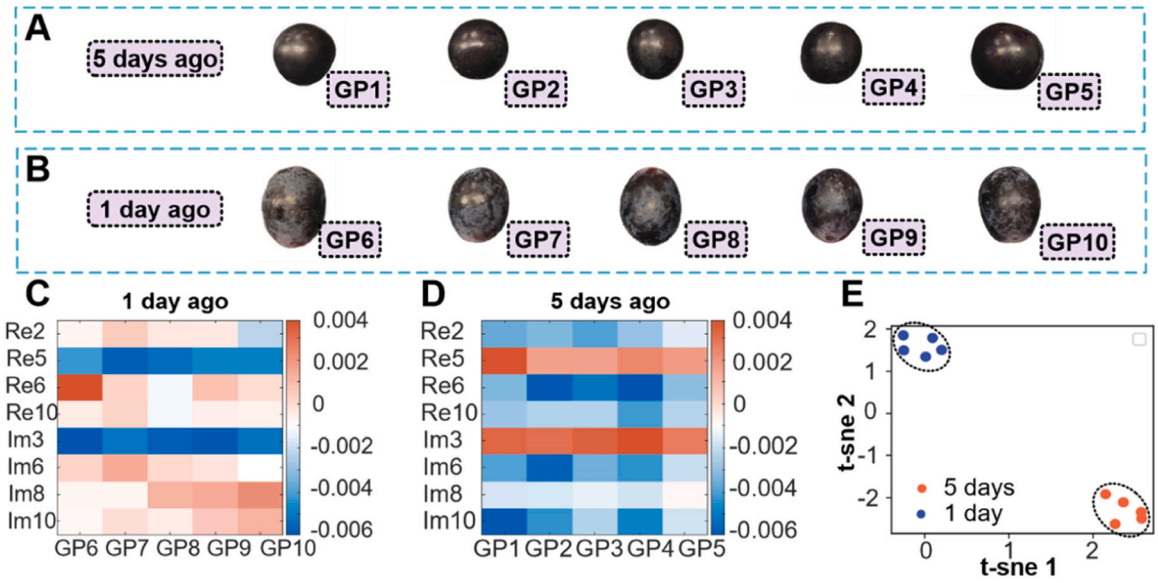

Fig. 7. A) Grapes bought 5 days before measurement. B) Grapes bought 1 day before measurement. C) Heatmap made up of eight selected features for one-day ago Grapes. D) Heatmap for five-days ago Grapes. E) t-SNE results with clear separation between two groups of Grapes.

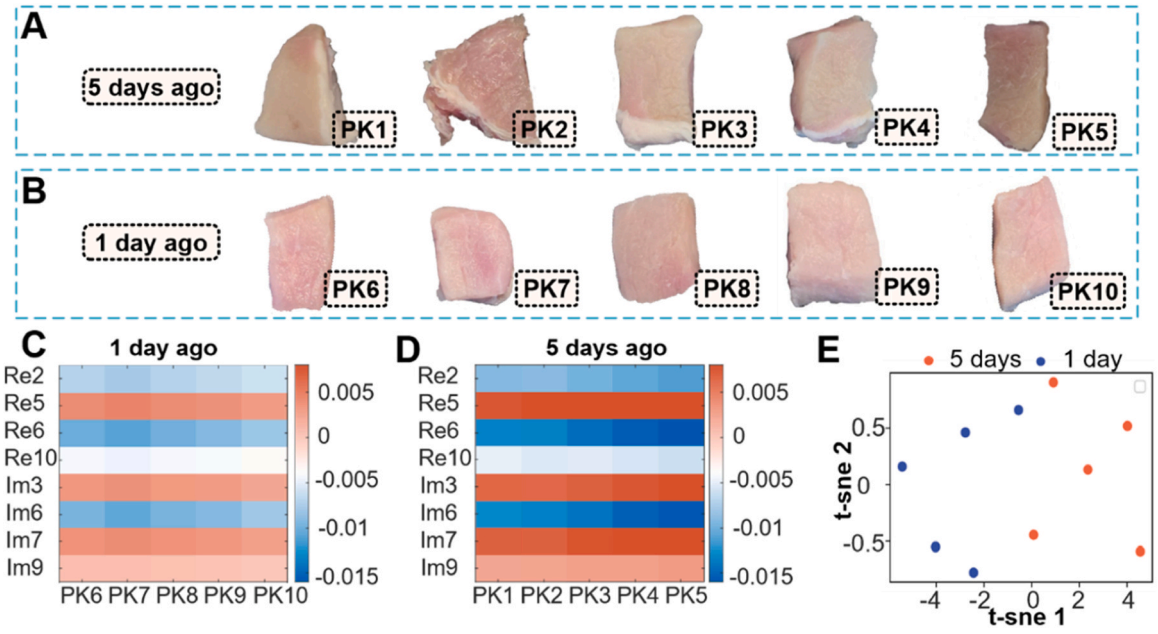

Fig. 8. A) Pork bought 5 days before measurement. B) Pork bought 1 day before measurement. C) Heatmap made up of eight selected features for one-day ago Pork. D) Heatmap for five-days ago Pork. E) t-SNE results with clear separation between two groups of Pork.

sensing operations.

Fig. 9D displays the 3D radiation pattern at 5.72 GHz with a measured realized gain of 5 dBi. The 2D radiation pattern in Fig. 9E agrees well with simulation. In Fig. 9F, simulated realized gain variation with nanomaterial characteristic at the communication frequency keep stable, emphasizing minimal impact on communication performance. Furthermore, the electric field distribution on the Ant-nose surface is shown in Fig. 9G to unravel the mechanism behind the high isolation between communication and sensing. At the communication resonance (5.72 GHz), energy concentrates on the slot dipole, while at 2.77 GHz and 4.76 GHz, it centers on interdigital finger (IDF1), where the nanomaterial is, indicating resonance induction by the RLC resonator. In summary, our dual-functional Ant-nose, operating independently for communication and sensing with a shared input port on a compact PCB, ensures consistent wireless performance for practical applications.

4. Conclusion

This work highlights the efficacy of a single antenna sensor coated with commercial nanomaterial, offering comparable performance and superior VOC isomer detection compared to sensor arrays. Utilizing a single microwave multi-resonant antenna with commercial GO and Nafion, our Ant-nose operates at room temperature, streamlining the system by eliminating the need for multiple sensors, various nanomaterials, multichannel data acquisition, additional supporting circuitry and heaters.

A diverse set of features in the reflection coefficient of Ant-nose is collected across an ultra-wide microwave band to ensure a

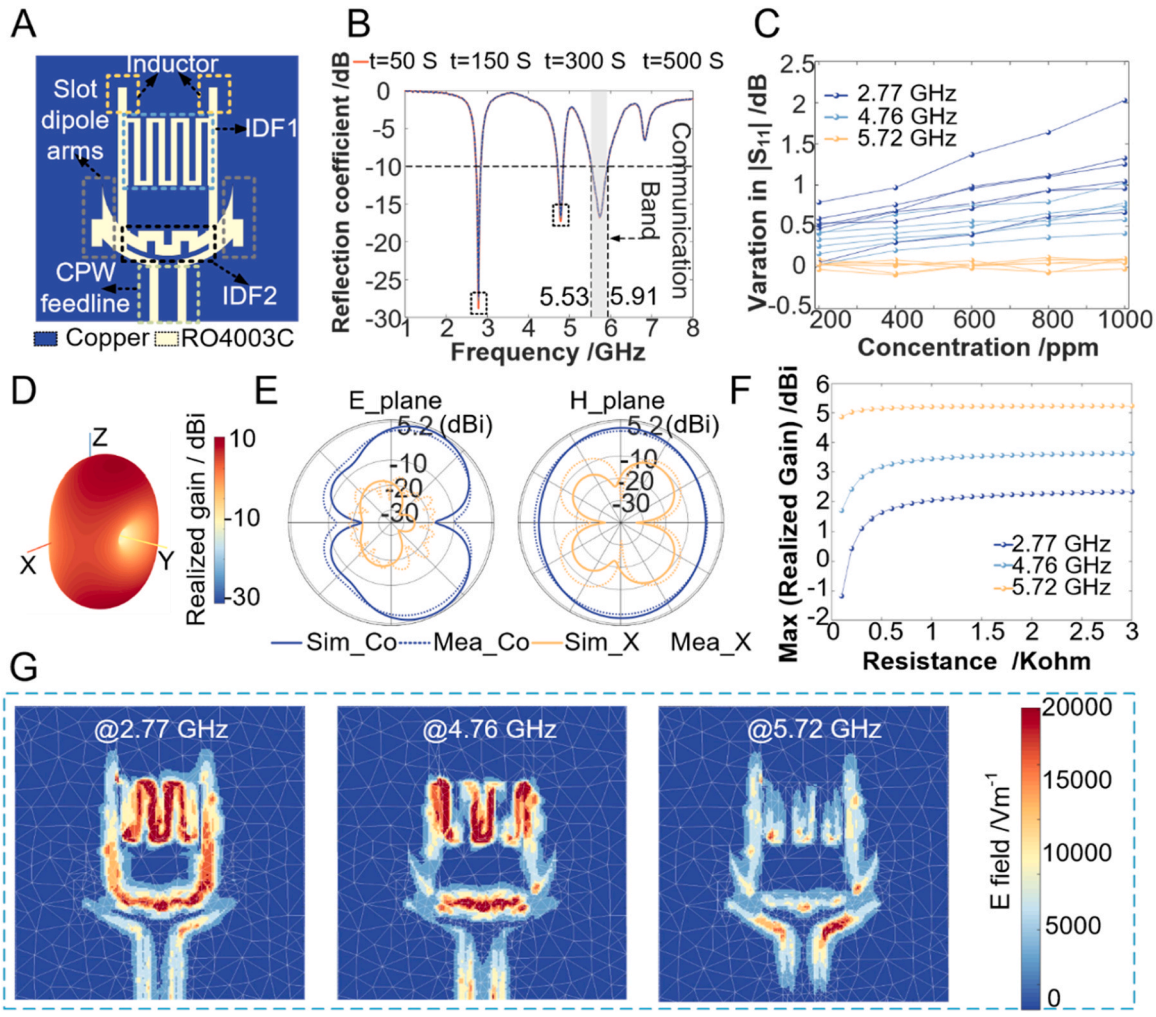

Fig. 9. A) Structure of the proposed novel microstripe antenna, where the corresponding function/equivalent structure of the microstrip configuration is highlighted by different colored boxes. B) Reflection coefficient (|S11|) of the proposed Ant-nose during the detection of 1000 ppm EtOH, illustrating four distinct sensing operation times represented by curves in different colors. C) Amplitude of the reflection coefficient at three different resonances varying with VOC concentration. Six lines in the same color represent six different VOC types (MeOH, PrOH, IPA, BuOH, 2-BuOH, and EtOH). D) Radiation pattern in 3D polar coordinate. E) Comparison of simulated and measured radiation pattern on E- and H-planes. Co for co-polarization and X for cross-polarization. F) Maximum realized gain at different resonaces as a function of nanomaterial resistance. G) Electric field distribution on the surface of the Ant-nose at three different resonances.

comprehensive VOC analyte fingerprint. Leveraging the XGBoost classification model, we achieved 100 % identification accuracy for four VOCs without isomers (MeOH, PrOH, BuOH, and EtOH), and 96.7 % for six VOCs with isomers (MeOH, PrOH, IPA, 2-BuOH, BuOH, and EtOH). Additionally, precise concentration estimates are obtained for each VOC using linear regression with R-squared values surpassing 0.99. Furthermore, our custom Transformer model accurately determined the concentration of elements in binary VOC isomer mixtures, achieving R-squared values greater than 0.98 for both 1/2-propanol and 1/2-butanol mixtures. Table S4 compares the performance of our Ant-nose with state-of-the-art sensor array-based e-noses, showcasing that Ant-nose's simplicity does not compromise performance. In terms of VOC isomer (even blend) identification and classification accuracy, Ant-nose outperforms other array-based e-noses.

Afterwards a series of real-life application scenarios, where multiple VOC species coexist, such as storage of grape, strawberry and pork, and mechanical damage of apple in supply chain, are checked separately. The clear visual separation between test and control group validates the feasibility of Ant-nose in practical complex applications. As a communication antenna, Ant-nose exhibits highly stable communication performance in terms of both frequency band and realized gain, regardless of the type or concentration of the VOC under test. Thus, our Ant-nose offers a new promising solution to develop low-cost and facile e-nose following simple procedure without compromising performance, which signifies an important step toward practical application of e-nose in IoT and wireless sensor network.

CRediT authorship contribution statement

Michael Cheffena: Writing – review & editing, Writing – original draft, Supervision, Software, Resources, Project administration, Methodology, Funding acquisition, Conceptualization. **Yenugu Veera Manohara Reddy:** Writing – review & editing, Writing – original draft, Visualization, Validation, Methodology, Investigation, Conceptualization. **Yu Dang:** Writing – review & editing, Writing – original draft, Visualization, Validation, Methodology, Investigation, Formal analysis, Data curation, Conceptualization.

Declaration of Competing Interest

The authors declare that they have no known competing financial interests or personal relationships that could have appeared to influence the work reported in this paper.

Data availability

Data will be made available on request.

Acknowledgements

The work is supported by the Norwegian University of Science and Technology (NTNU).

Appendix A. Supporting information

Supplementary data associated with this article can be found in the online version at doi:10.1016/j.snb.2024.136409.

References

[1] Z. Li, R. Paul, T. Ba Tis, A.C. Saville, J.C. Hansel, T. Yu, J.B. Ristaino, Q. Wei, Non-invasive plant disease diagnostics enabled by smartphone-based fingerprinting of leaf volatiles, Nat. Plants 5 (2019) 856–866.
[2] P. Cui, G. Schito, Q. Cui, Voc emissions from asphalt pavement and health risks to construction workers, J. Clean. Prod. 244 (2020) 118757.
[3] K. Liu, C. Zhang, Volatile organic compounds gas sensor based on quartz crystal microbalance for fruit freshness detection: a review, Food Chem. 334 (2021) 127615.
[4] L. Guo, T. Wang, Z. Wu, J. Wang, M. Wang, Z. Cui, S. Ji, J. Cai, C. Xu, X. Chen, Portable foodfreshness prediction platform based on colorimetric barcode combinatorics and deep convolutional neural networks, Adv. Mater. 32 (2020) 2004805.
[5] T. Bruderer, T. Gaisl, M.T. Gaugg, N. Nowak, B. Streckenbach, S. Muller, A. Moeller, M. Kohler, R. Zenobi, On-line analysis of exhaled breath: focus review, Chem. Rev. 119 (2019) 10803–10828.
[6] Y. Geng, M.A. Ali, A.J. Clulow, S. Fan, P.L. Burn, I.R. Gentle, P. Meredith, P. E. Shaw, Unambiguous detection of nitrated explosive vapours by fluorescence quenching of dendrimer films, Nat. Commun. 6 (2015) 8240.
[7] Z.-F. Zhang, X. Zhang, X.-M. Zhang, L.-Y. Liu, Y.-F. Li, W. Sun, Indoor occurrence and health risk of formaldehyde, toluene, xylene and total volatile organic compounds derived from an extensive monitoring campaign in harbin, a megacity of china, Chemosphere 250 (2020) 126324.
[8] A. Martínez, A. Hernández, C. Moraga, P. Tejero, M. de Gúia Córdoba, A. Martín, Detection of volatile organic compounds associated with mechanical damage in apple cv.'golden delicious' by headspace solid-phase microextraction (hs-spme) and gc-ms analysis, LWT 172 (2022) 114213.
[9] C. Taiti, C. Costa, P. Menesatti, S. Caparrotta, N. Bazihizina, E. Azzarello, W. A. Petrucci, E. Masi, E. Giordani, Use of volatile organic compounds and physicochemical parameters for monitoring the post-harvest ripening of imported tropical fruits, Eur. Food Res. Technol. 241 (2015) 91–102.
[10] Z. Li, Y. Liu, O. Hossain, R. Paul, S. Yao, S. Wu, J.B. Ristaino, Y. Zhu, Q. Wei, Real-time monitoring of plant stresses via chemiresistive profiling of leaf volatiles by a wearable sensor, Matter 4 (2021) 2553–2570.
[11] J.S. Weerakkody, M. El Kazzy, E. Jacquier, P.-H. Elchinger, R. Mathey, W.L. Ling, C. Herrier, T. Livache, A. Buhot, Y. Hou, Surfactant-like peptide self-assembled into hybrid nanostructures for electronic nose applications, ACS Nano 16 (2022) 4444–4457.
[12] F. Röck, N. Barsan, U. Weimar, Electronic nose: current status and future trends, Chem. Rev. 108 (2008) 705–725.
[13] W. Hu, L. Wan, Y. Jian, C. Ren, K. Jin, X. Su, X. Bai, H. Haick, M. Yao, W. Wu, Electronic noses: from advanced materials to sensors aided with data processing, Adv. Mater. Technol. 4 (2019) 1800488.
[14] S. Deshmukh, R. Bandyopadhyay, N. Bhattacharyya, R. Pandey, A. Jana, Application of electronic nose for industrial odors and gaseous emissions measurement and monitoring–an overview, Talanta 144 (2015) 329–340.
[15] N.S. Capman, X.V. Zhen, J.T. Nelson, V.S.K. Chaganti, R.C. Finc, M.J. Lyden, T. L. Williams, M. Freking, G.J. Sherwood, P. Buhlmann, Machine learning-based rapid detection of volatile organic compounds in a graphene electronic nose, ACS Nano 16 (2022) 19567–19583.
[16] N.J. Kybert, G.H. Han, M.B. Lerner, E.N. Dattoli, A. Esfandiar, A. Charlie Johnson, Scalable arrays of chemical vapor sensors based on dna-decorated graphene, Nano Res. 7 (2014) 95–103.
[17] T. Wang, H. Ma, W. Jiang, H. Zhang, M. Zeng, J. Yang, X. Wang, K. Liu, R. Huang, Z. Yang, Type discrimination and concentration prediction towards ethanol using a machine learning–enhanced gas sensor array with different morphology-tuning characteristics, Phys. Chem. Chem. Phys. 23 (2021) 23933–23944.
[18] M. Kang, I. Cho, J. Park, J. Jeong, K. Lee, B. Lee, D. Del Orbe Henriquez, K. Yoon, I. Park, High accuracy real-time multi-gas identification by a batch-uniform gas sensor array and deep learning algorithm, ACS Sens 7 (2022) 430–440.
[19] K. Lee, I. Cho, M. Kang, J. Jeong, M. Choi, K.Y. Woo, K.-J. Yoon, Y.-H. Cho, I. Park, Ultralow-power e-nose system based on multi-micro-led-integrated, nanostructured gas sensors and deep learning, ACS Nano 17 (2022) 539–551.
[20] Y. Ravi Kumar, K. Deshmukh, T. Kovářík, S.K. Khadheer Pasha, A systematic review on 2d materials for volatile organic compound sensing, Coord. Chem. Rev. 461 (2022) 214502.
[21] C. Zhang, Z.-L. Hou, B.-X. Zhang, H.-M. Fang, S. Bi, High sensitivity self-recovery ethanol sensor based on polyporous graphene oxide/melamine composites, Carbon 137 (2018) 467–474.
[22] G. Thangamani, K. Deshmukh, T. Kovářík, N. Nambiraj, D. Ponnamma, K. K. Sadasivuni, H.A. Khalil, S.K. Pasha, Graphene oxide nanocomposites based room temperature gas sensors: a review, Chemosphere 280 (2021) 130641.
[23] F. Yin, W. Yue, Y. Li, S. Gao, C. Zhang, H. Kan, H. Niu, W. Wang, Y. Guo, Carbon-based nanomaterials for the detection of volatile organic compounds: a review, Carbon 180 (2021) 274–297.
[24] M.G. Mayani, F.J. Herraiz-Martínez, J.M. Domingo, R. Giannetti, Resonator-based microwave metamaterial sensors for instrumentation: survey, classification, and performance comparison, IEEE Trans. Instrum. Meas. 70 (2020) 1–14.
[25] H. Huang, Flexible wireless antenna sensor: a review, IEEE Sens. J. 13 (2013) 3865–3872, https://doi.org/10.1109/JSEN.2013.2242464.
[26] Q. Zhang, Y. Wang, D. Li, J. Xie, K. Tao, P. Hu, J. Zhou, H. Chang, Y. Fu, Multifunctional and wearable patches based on flexible piezoelectric acoustics for integrated sensing, localization, and underwater communication, Adv. Funct. Mater. 33 (2023) 2209667.
[27] T. Alam, M. Cheffena, Integrated microwave antenna/sensor for sensing and communication applications, IEEE Trans. Microw. Theory Tech. 70 (2022) 5289–5300, https://doi.org/10.1109/TMTT.2022.3199242.
[28] T. Alam, M. Cheffena, E. Rajo-Iglesias, Dual-functional communication and sensing antenna system, Sci. Rep. 12 (2022) 20387.
[29] X. Leng, D. Luo, Z. Xu, F. Wang, Modified graphene oxide/nafion composite humidity sensor and its linear response to the relative humidity, Sens. Actuators B Chem. 257 (2018) 372–381.
[30] L. Estevez, A. Kelarakis, Q. Gong, E.H. Da'as, E.P. Giannelis, Multifunctional graphene/platinum/nafion hybrids via ice templating, J. Am. Chem. Soc. 133 (2011) 6122–6125, https://doi.org/10.1021/ja200244s.
[31] D. Li, B. Zhu, K. Pang, Q. Zhang, M. Qu, W. Liu, Y. Fu, J. Xie, Virtual sensor array based on piezoelectric cantilever resonator for identification of volatile organic compounds, ACS Sens 7 (2022) 1555–1563.
[32] D. Li, G. Liu, Q. Zhang, M. Qu, Y.Q. Fu, Q. Liu, J. Xie, Virtual sensor array based on mxene for selective detections of vocs, Sens. Actuators B Chem. 331 (2021) 129414.
[33] D. Li, Z. Xie, M. Qu, Q. Zhang, Y. Fu, J. Xie, Virtual sensor array based on butterworth–van dyke equivalent model of qcm for selective detection of volatile organic compounds, ACS Appl. Mater. Interfaces 13 (2021) 47043–47051.
[34] B. Ding, X. Wang, J. Yu, M. Wang, Polyamide 6 composite nano-fiber/net functionalized by polyethyleneimine on quartz crystal microbalance for highly sensitive formaldehyde sensors, J. Mater. Chem. 21 (2011) 12784–12792.
[35] T. Cowen, M. Cheffena, Molecularly imprinted polymer real-time gas sensor for ambient methanol vapor analysis developed using principles of sustainable chemistry, ACS Sustain. Chem. Eng. 11 (2023) 10598–10604.
[36] K. Hossain, T. Cowen, M. Cheffena, Molecularly imprinted polymer based antenna sensor for methanol vapor sensing, IEEE Microw. Wirel. Technol. Lett. (2023).
[37] D. Li, W. Liu, B. Zhu, M. Qu, Q. Zhang, Y. Fu, J. Xie, Machine learning-assisted multifunctional environmental sensing based on a piezoelectric cantilever, ACS Sens 7 (2022) 2767–2777.
[38] M. Tonezzer, J.-H. Kim, J.-H. Lee, S. Iannotta, S.S. Kim, Predictive gas sensor based on thermal fingerprints from pt-sno2 nanowires, Sens. Actuators B Chem. 281 (2019) 670–678.
[39] P. Qin, B.A. Day, S. Okur, C. Li, A. Chandresh, C.E. Wilmer, L. Heinke, Voc mixture sensing with a mof film sensor array: detection and discrimination of xylene isomers and their ternary blends, ACS Sens 7 (2022) 1666–1675.
[40] M. Khatib, T.-P. Huynh, J.J. Sun, T.T. Do, P. Sonar, F. Hinkel, K. Mullen, H. Haick, Organic transistor based on cyclopentadithiophene-benzothiadiazole donor–acceptor copolymer for the detection and discrimination between multiple structural isomers, Adv. Funct. Mater. 29 (2019) 1808188.
[41] M.M. Ali, N. Hashim, S. Abd Aziz, O. Lasekan, Principles and recent advances in electronic nose for quality inspection of agricultural and food products, Trends Food Sci. Technol. 99 (2020) 1–10.
[42] S. Tiwari, A. Kate, D. Mohapatra, M.K. Tripathi, H. Ray, A. Akuli, A. Ghosh, B. Modhera, Volatile organic compounds (vocs): biomarkers for quality management of horticultural commodities during storage through e-sensing, Trends Food Sci. Technol. 106 (2020) 417–433.
[43] D. Zhu, X. Ren, L. Wei, X. Cao, Y. Ge, H. Liu, J. Li, Collaborative analysis on difference of apple fruits flavour using electronic nose and electronic tongue, Sci, Hortic 260 (2020) 108879.
[44] L. Wu, J. He, G. Liu, S. Wang, X. He, Detection of common defects on jujube using vis-nir and nir hyperspectral imaging, Postharvest Biol. Technol. 112 (2016) 134–142.
[45] U.L. Opara, P.B. Pathare, Bruise damage measurement and analysis of fresh horticultural produce—a review, Postharvest Biol. Technol. 91 (2014) 9–24.
[46] R. Dhital, P. Joshi, N. Becerra-Mora, A. Umagiliyage, T. Chai, P. Kohli, R. Choudhary, Integrity of edible nano-coatings and its effects on quality of strawberries subjected to simulated in-transit vibrations, LWT 80 (2017) 257–264.
[47] T. Fadiji, C. Coetzee, P. Pathare, U.L. Opara, Susceptibility to impact damage of apples inside ventilated corrugated paperboard packages: effects of package design, Postharvest Biol. Technol. 111 (2016) 286–296.
[48] X. Lu, G. Meng, W. Jin, H. Gao, Effects of 1-mcp in combination with ca application on aroma volatiles production and softening of 'fuji'apple fruit, Sci. Hortic. 229 (2018) 91–98.
[49] C. Besada, A. Salvador, S. Sdiri, R. Gil, A. Granell, A combination of physiological and chemometrics analyses reveals the main associations between quality and

ripening traits and volatiles in two loquat cultivars, Metabolomics 9 (2013) 324–336.
[50] E.G. Vilar, M.G. O'Sullivan, J.P. Kerry, K.N. Kilcawley, Volatile organic compounds in beef and pork by gas chromatography-mass spectrometry: a review, Sep. Sci. 5 (2022) 482–512.
[51] A. Morales-Fernandez, M. Fernandez-Barciela, F. Isasi-Vicente, F. Martin-Rodriguez, P.J. Tasker, Dual-band class j power amplifier at 2.45 and 5.8 ghz for uavs communications, IEEE Access 10 (2022) 48673–48680.
[52] Z.X. Xia, K.W. Leung, M.W.K. Lee, N. Yang, Miniature dual-band meander-line monopole chip antenna with independent band control, IEEE, Antennas Wirel. Propag. Lett. 18 (2019) 1873–1877.
[53] W. Stevers, A. Schlegel, P. Chatterjee, J. Opperman, J.A. Nanzer, Direction-of-arrival estimation using a low-cost, portable, software-defined-radio-based phase interferometry system, IEEE Antennas Propag. Mag. 61 (2019) 78–84.

Yu Dang received the B.S. degree in microwave technology and the M.S. degree in microwave technology from the Harbin Institute of Technology, in 2017 and 2019, respectively. He is currently pursuing his PhD degree under the supervision of Prof. Cheffena at the Norwegian University of Science and Technology (NTNU), Norway. His research interests include 5 G antenna sensor, E-nose, metasurface-based microwave imaging, and MIMO antenna.

Yenugu Veera Manohara Reddy is an Assistant Professor in the Department of Chemistry at Sri Venkateswara College, University of Delhi. He earned his Ph.D. in Chemistry from Sri venkateswara University, specializing in Material Chemistry, Electrochemistry, and Energy Storage Applications. During his postdoctoral tenure at Chung Ang University, South Korea, he played a pivotal role in the project "Development of MXene-based nanobiosensors for the detection of influenza virus." Dr. Reddy's international exposure extends to his position as a Postdoctoral Researcher at the Norwegian University of Science and Technology (NTNU), Norway, where he focused on developing flexible 5 G antenna sensor arrays and inkjet-printed MXene electrodes. Additionally, he served as a Research Assistant Professor at Gachon University, South Korea, contributing to the development of MOFs and boron nitride nanotubes. Dr. Reddy's diverse research interests encompass wearable electrochemical biosensors, nanosensors, disease diagnostics, and molecular diagnostics. His prolific publication record includes numerous research papers in high-impact journals.

Michael Cheffena received the M.Sc. degree in electronics and computer technology from the University of Oslo, Oslo, Norway, in 2005, and the Ph.D. degree from the Norwegian University of Science and Technology (NTNU), Trondheim, Norway, in 2008 In 2007, he was a Visiting Researcher at the Communications Research Center, Ottawa, ON, Canada. From 2009–2010, he conducted a postdoctoral study at the University Graduate Center, Kjeller, Norway, and the French Space Agency, Toulouse, France. He is currently a Full Professor at NTNU, Gjøvik, Norway. His research interests include the modeling and prediction of propagation radio channels, signal processing, medium access control protocol design, antenna sensors, and sensor systems.